Cement and Concrete Research 41 (2011) 817–827

Contents lists available at ScienceDirect

Cement and Concrete Research

journal homepage: http://ees.elsevier.com/CEMCON/default.asp

Toward a better comprehension and modeling of hysteresis cycles in the water sorption–desorption process for cement based materials

H. Ranaivomanana [a,*], J. Verdier [a], A. Sellier [a], X. Bourbon [b]

[a] Université de Toulouse, UPS, INSA, LMDC (Laboratoire Matériaux et Durabilité des Constructions), 135, Avenue de Rangueil, F-31 077 Toulouse Cedex04, France
[b] Andra, Parc de la Croix Blanche, 1-7 Rue Jean Monnet, F-92 298 Chatenay Malabry Cedex, France

ARTICLE INFO

Article history:
Received 18 March 2010
Accepted 21 March 2011

Keywords:
Drying (A)
Adsorption (C)
Cycles (C)
Permeability (C)
Cementitious materials

ABSTRACT

The aim of this work is to describe a method based on a simple representation of the pore size distribution, which is able to predict hysteresis phenomena encountered in water sorption–desorption isotherms, particularly for cementitious materials. The hysteresis effect due to network constrictivity is taken into account in order to extend models of transfer in porous media to situations involving wetting–drying cycles. This is not achieved in earlier models and their performance in terms of prediction in such conditions is thus limited. The present modeling is based on an idealized pore size distribution. This has three modes, associated with C–S–H pores, medium capillary pores, and large capillary pores including consideration of cracks. The distribution is assessed from the chemical composition of the cement, the formulation of the material, the degree of hydration, the total water porosity and the intrinsic permeability.

1. State of the art

The modeling of transfer properties through porous media is a widely studied topic, especially in the field of civil engineering with cementitious materials. Pore network models have been developed to assess the liquid and gas permeability [1–6] and the water diffusivity of such materials [7,8], to simulate mercury intrusion [9] or to study the kinetics of capillary imbibition [10]. The aim of our study is to develop a physical model representing the hydric behavior of the porous space. As in previous work, our model is based on the size distribution of pores and can lead to an estimate of the water content of the material , whatever its humidity history. However the proposed study is not restricted to finding the sorption and desorption isotherms but also predicts the non-linear connecting paths anywhere between them. This non-linearity is due to hysteresis.

Aligizaki [11] describes the different types of hysteresis (de Boer classification [12] and IUPAC classification [13]) and the different theories on the origin of the hysteresis. The author mentions, among others, McBain [14] and Brunauer et al. [15]. Mc Bain explains the hysteresis effect by the presence of ink bottle pores. The wide part is filled at high relative humidity but can only be drained during desorption when the narrow part is at low relative humidity. Brunauer et al. [15] assumed that, for the same pore, capillary condensation and evaporation occurred at different relative humidities. Based on test results of nitrogen adsorption, Aligizaki [11] deduced that the shape of the hysteresis loop obtained on cement pastes was of the B or D type according to the classification of de Boer or the H3 type according to the IUPAC classification. This reflects the fact that the pores are composed of large capillaries with narrow necks or have flattened shapes (corresponding, for example, to the representation of the C–S–H gel structure in sheets). By performing several cycles of wetting–drying at different levels of relative humidity between 3% and 100% on various cementitious materials, Baroghel Bouny [16,17] infers that hysteresis is present throughout this range of relative humidity. It is significant between 33% RH and 100% RH and the author attributes its origin to the difference between the mechanisms of condensation and evaporation due to the shape of the pores or to the possible presence of different shapes in the liquid–vapor interface. For low RH (RH <33%), a change of microstructure due to the departure of water strongly bound to the C–S–H explains the hysteresis. Other possible causes cited by the author are the presence of “multi-scale ink-bottle pores” or “kinetic effects” which complicate and delay the establishment of balance especially in the median range of RH where moisture transport is slower due to the discontinuity of the liquid phase. Also according to Baroghel Bouny [16], the hysteresis effect is a short-term phenomenon corresponding to a thermodynamically unstable condition and should subside and disappear after a certain period of time depending on the temperature and relative humidity range. This is confirmed by other researchers, e.g. Ishida et al. [18], who suggest a gradual dispersion of water in the ink bottle pores under the effect of temperature. In a recent publication, Poyet [19] uses the heat involved in the exothermic adsorption process to explain the effect of temperature on the first desorption isotherm. An increase in temperature hinders the process, decreasing the number of adsorbed molecules and therefore the water content. Conversely, the desorption process is encouraged. Espinosa and Franke [20] explain hysteresis by the fact that the pores affected by capillary condensation

---

[*] Corresponding author. Tel.: +33 5 61 55 99 93; fax: +33 5 61 55 99 49.
E-mail address: hranaivo@insa-toulouse.fr (H. Ranaivomanana).

0008-8846/$ – see front matter © 2011 Elsevier Ltd. All rights reserved.
doi:10.1016/j.cemconres.2011.03.012

are not the same as those affected by desorption for a given relative humidity, when they are accessible at both ends. Capillary condensation takes place without the formation of a meniscus at the liquid–vapor interface (cylindrical). In contrast, menisci appear before desorption takes place. In the case where the pores are accessible only by one end, a meniscus takes form at the liquid–vapor interface in both capillary condensation and desorption. The pore radii involved in both processes are then the same, preventing hysteresis. The authors also associate the hysteresis effect with a modification of the porous structure at the end of desorption due to the drying mode (by drying at 105 °C or freeze–drying). The effect of the degree of hydration of the cement, which continues to evolve during the tests, is also mentioned.

The models already developed to describe the porous space and simulate moisture transfer in particular for cementitious materials, do not especially include the hysteresis effect. Philippi and Souza [21] propose a 3-scale geometric model of the porous structure of cement and lime mortar in order to study the influence of the model on the simulation of moisture retention and transfer. Bary [22] implements a network model based on pore size distribution to describe moisture transfer in cement-based materials. It is a probabilistic model assimilating porosity to a system of overlapping spheres. With this model, the author connects the degree of saturation with pore size. The relationship obtained is then used with the Kelvin–Laplace law to obtain the isotherm.

Generally, when hysteresis is taken into account, the basic principle is always the same. A pore is assumed saturated if its radius is smaller than that obtained by the Kelvin–Laplace. Due to the network constrictivity, this pore is connected to others (with radii larger than that obtained by the Kelvin–Laplace) which remain also saturated. The difference between the proposed approaches lies mainly in the representation of the pore space and therefore the implementation of the model. A probabilistic 2D model of a multi-scale porous network is suggested by Carmeliet et al. [23]. Although their model is able to correctly reproduce the hysteresis, it was developed for materials with a broad pore size distribution composed of only two families. The first was chosen with an equivalent radius equal to or greater than 1000 nm and the second with an equivalent radius between 1 nm and 1000 nm, which is not sufficient to describe cementitious materials. The 3D porous network version of the model is also widely used. It consists of two entities: sites (spherical cavities) interconnected by links (cylindrical pores), each with its own size distribution. Other approaches involve the concept of mathematical morphology (shape description) [24,25]. However, for those models, the list of which is not exhaustive, the relevance to cementitious materials is ignored because they were tested for other types of materials.

In the model developed for cementitious materials, Sallee and Quenard [26] address the study of water vapor transfer mechanisms in microporous materials using a hierarchical approach with three levels: microscopic (cylindrical shaped pore), microstructure (simplified representation of the microstructure from network models with a well defined topology) and mesoscopic. The set allows sorption isotherms and vapor permeability to be estimated. In their modeling, the hysteresis effect is taken into account by the fact that a pore can only be desaturated if it has access to a continuous path of air connected to the accessible network. This allows the ink bottle effect, which becomes accentuated when the network is poorly connected, to be integrated. However, besides the fact that the results of the model had not been confronted with experimental results to verify its relevance, it was also tested for only one cycle involving desorption until the dry state was reached. Espinosa and Franke [27] have developed a method to predict the isotherms for cement pastes and mortars. They combine a thermodynamic model of molecular adsorption in porous materials with a cylindrical pore model including ink-bottle pores in order to consider their influence on the hysteresis effect. Ishida, Kishi and Maekawa, [18–28] propose a model of moisture transfer taking the effect of temperature into account. In their modeling, they develop a pore size distribution model (Rayleigh Ritz distribution) able to take account of the hysteresis effect to simulate sorption and desorption isotherms. A residual saturation, noted as S_{ink}, remaining in the pores assumed to be already drained due to the “ink-bottle” effect, is considered on the pore size distribution as shown in Fig. 1.

Without questioning the models mentioned above, especially those developed for cementitious materials, it nevertheless remains true that their performance in predicting isotherms with particular consideration of the hysteresis effect is uncertain. This is the reason why we propose some improvements to earlier models, for the management of the hysteresis cycles. The experimental program implemented to obtain complete data sets is presented first and the modeling is discussed afterwards.

2. Experimental program

2.1. Program objectives

The bases of the model proposed in this study were established from the results of isotherm tests that we carried out for the same reason. Experimental results from the literature were also used. The materials studied and the main experimental results are described below.

2.2. Materials

The tests were performed on two concretes, denoted C1 and C2, made respectively with Ordinary Portland Cement (OPC) and Portland Slag Fly ash Cement. These are the concrete formulations envisioned by Andra for nuclear waste repository structures in deep geologic formations. Isotherms obtained by Hyvert [29] on a OPC-based mortar, denoted M, and the results obtained by Baroghel Bouny [17] on OPC-based cement pastes (formulations CP1 and CP2) were also used to evaluate the model. The chemical compositions of the cements used in each mortar or concrete test specimen are given in Table 1. The formulation of the various materials and their physical characteristics are in Table 2. For porosity and bulk density measurements, the samples were saturated under vacuum for at least 24 h, then weighted in water and in air to determine their volume, and dried at 105 °C to constant mass. For the case of cement paste CP2, the bulk density was not measured but estimated from the amount of hydrates formed by using Eq. (2). The degree of hydration was computed to 80% by Camps [30] for concrete C1 and 72% for concrete C2. For cement pastes CP1 and CP2, Baroghel Bouny [17] measured respectively 0.76 and 0.9. Nevertheless, we find that these values are slightly overestimated. Generally, the cement never reaches a complete hydration especially in the case of low water/cement ratio because the accessibility of water to anhydrous

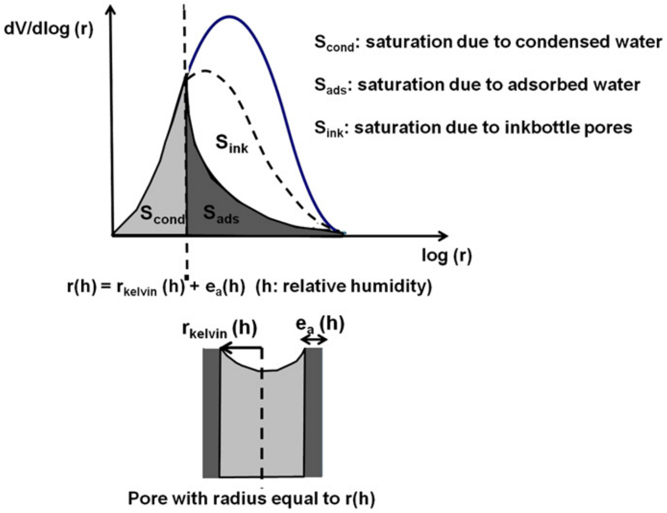

Fig. 1. Hysteresis modeling inspired from [18–28].

Table 1
Chemical compositions of cements used in each test specimen.

(% by weight)	Test specimens				
	C1	C2	M	CP1	CP2
SiO_2	20.90	26.88	20.10	22.72	23.44
Al_2O_3	3.20	9.71	4.90	5.16	2.74
Fe_2O_3	4.60	2.91	3.50	2.33	2.50
CaO	65.10	50.74	63.60	64.43	66.20
MgO	0.60	2.73		1.21	0.80
SO_3	2.76–3.00	2.69	3.50	2.86	2.04
Na_2O	0.10	0.20	0.10	0.18	0.43
K_2O	0.60	1.06	1.60	0.44	0.43

grains becomes reduced during hydration. According to the formula (Eq. (1)) proposed by Waller [31], the degrees of hydration are respectively estimated at 68% for cement paste CP1, 77% for cement paste CP2 and 80% for mortar M.

$$\alpha = 1 - \exp(-3.3 \times {}^{w}/{}_{c}) \qquad (1)$$

Where α is the hydration degree and w/c is the water/cement ratio (kg/kg).

The model proposed in the second part considers a partition of porosity between C–S–H pores and capillary pores. For this, we must determine the amount of C–S–H formed after hydration. Powers and Brownyard [32], make the assumption that the porosity of C–S–H is independent of the degree of hydration and of the water/cement ratio. It is constant and equal to about 28%. This intrinsic value of C–S–H porosity was recently highlighted by Baroghel Bouny [16] from water vapour sorption isotherms. It was also adopted by Maekawa et al. [28] in their pore structure model of cement paste. The volume of capillary pores occupied by water not consumed by the hydration is obtained from the difference between the volumes of water and cement initially present in the paste and the volumes of hydrates formed and of anhydrated cement. To calculate the volume of C–S–H, we used the approach proposed by Adenot [33] and adopted by Bary and Sellier [34], using as input the chemical composition of the cement, the formulation of the material and the degree of hydration (Tables 1 and 2).

In the case of a material made with OPC, the phases composing the cement matrix are given in Table 3.

Authors such as Richardson [35] have shown for C–S–H that the average value of the C/S ratio is around 1.7. This was confirmed recently by Nguyen [36].

The amount of hydrates formed is related to the components of anhydrated cement (CaO, SiO_2, Al_2O_3, SO_3) by the following system of equations

$$\begin{aligned} CaO &= CH + 1.7CSH + 4AFm + 6AFt(\text{or}\,3C_3AH_6) \\ SiO_2 &= CSH \\ 2Al_2O_3 &= AFt(\text{or}\,2C_3AH_6) + AFm \\ SO_3 &= 3AFt(\text{or}\,0C_3AH_6) + AFm \end{aligned} \qquad (2)$$

Table 3
Hydrates composing the cement matrix.

	Chemical formula	Notation
Portlandite	$Ca(OH)_2$	CH
C–S–H	$1.7CaO.SiO_2.2.45H_2O$	C–S–H
Monosulfate	$3CaO.Al_2O_3.CaOSO_3.12H_2O$	AFm
Ettringite/ hexahydrate	$3CaO.Al_2O_3.3CaOSO_3.32H_2O/3CaO.Al_2O_3.6H_2O$	AFt/C_3AH_6

This approach is suitable for OPC not for slag or fly ash for instance.

The molar volumes of the different phases are given in Table 4 below

In the case of a material made with cement with slag and fly ash additions, we have to take into account the pozzolanic reactions. In fact, the portlandite formed during the hydration of clinker reacts with silica of slag not consumed during its hydration and silica contained in fly ash. The reaction leads to the formation of secondary C–S–H. Their C/S ratio is close to 1 because they occur during the hydration phase, when calcium ions start to lack from the pore water [28]. We approach the hydration of Portland–Slag–Fly ash-cement by considering first the hydration of clinker, then hydration of slag. The last step is the pozzolanic reaction of fly ash. In our approach, kinetics of the reactions are not considered but only the quantities of each element which react. These quantities are evaluated from the "mean" value of the hydration degree: 72% which is assumed to correspond to the stabilization of cement hydration. Of course, the approach stays approximate because it is a simplified view of blended cement hydration. We assume that the porosity of C–S–H formed during the hydration of clinker and the porosity of secondary C–S–H are almost the same, i.e. about 28%. The amount of C–S–H and the distribution of pore volume for 1 m^3 of material are given in Table 5. The amounts of C–S–H are computed by using Eq. (2). By multiplying the obtained values by the intrinsic porosity of C–S–H (equal to 28%), we obtain the volume of C–S–H pores. Thus, the volume of capillary pores is the remaining percentage required to reach the water porosity.

In the pore size classification proposed by Mindess et al. [38], the C–S–H gel pores are smaller than 10 nm. Thin capillaries are between 2.5 nm and 50 nm and large capillaries are between 50 nm and 10 μm. The entrapped air bubbles are classified between 100 μm and 1 mm. This pore size classification was adopted for our study. However we did not include entrained air bubbles because they are not totally accessible to water. They are also of little importance in terms of water transfer [11,17].

2.3. Tests

2.3.1. Isotherms

Sorption and desorption isotherms were experimentally obtained from 7 cm × 7 cm × 28 cm prismatic samples. The specimens C1 and C2 were removed from the moulds 24 hours after casting, covered

Table 2
Mix design and characteristics of test mixtures.

	C1	C2	M	CP1	CP2
Cement (kg/m^3)	400.00	450.00	400.00	1502.00	1306.00
Limestone sand 0/4 mm (kg/m^3)	858.00	800.00			
Siliceous sand (kg/m^3)			1212.00		
Limestone gravel 5/12.5 mm (kg/m^3)	945.00	984.00			
Superplasticizer (kg/m^3)	10.00	11.25			
Total water (kg/m^3)	178.00	183.00	200.00	523.00	588.00
Porosity (%)	12.30	14.70	17.20	30.30	40.50
Bulk density (kg/m^3)	2349.00	2291.00	2050.00	1717.00	1500.00
Hydration degree	0.80	0.72	0.80	0.76 (measured) 0.68 (estimated)	0.90 (measured) 0.77 (estimated)

Table 4
Molar volumes of different phases composing the cement matrix [37].

	CH	C–S–H	AFm	C_3AH_6
Molar volume (cm^3/mol)	33.1	88.1	313	150

with adhesive foil and stored in endogenous cure conditions in a temperature controlled room at 20 °C for one year. At the end of the curing time they were weighted and saturated under vacuum. They were weighted again (immersed and in air) to determine their apparent volume and to obtain their density after the endogenous cure. Then, the specimens were cut in wet conditions into 7 cm × 3.5 cm × 0.5 cm slices that were numbered and coated with resin on their sides. A thickness of 0.5 cm was chosen in order to reach the equilibrium quickly and to limit the test duration. After the setting of the resin (~12 h), the slices were then resaturated under vacuum and placed in sealed Plexiglas cells in which the relative humidity was controlled using saturated salt solutions placed in cups. The cells were regularly monitored with a thermo-hygrometer. A small fan ran continuously so as to homogenize the atmosphere in the cells. The cells were placed in a glove box, the role of which was to protect the samples from the atmospheric CO_2 as carbonation modifies the pore network and also the dried mass of the material. This precaution was associated with a regular sweep of nitrogen to remove all the CO_2. The amount of CO_2 remaining in the glove box after 24 hours without sweeping was always below 100 ppm. Specimen masses were monitored during testing using a balance with an accuracy of 1 mg. Equilibrium was reached when the mass of material did not vary by more than 0.01% between two successive weightings. For each level of imposed RH, the weights were measured daily during the first week, then once a week until equilibrium was reached. A mean value extracted from three samples was considered representative of the results, as shown in [16–20]. The different levels of relative humidity with the corresponding saline solutions were: 97% (potassium sulfate), 86% (potassium chloride), 76% (sodium chloride), 55% (dichromate potassium), 44% (potassium carbonate). To highlight the hysteresis effect on different relative humidity levels, four cycles were performed: the first three involved sorption from 76%, 55% and 44% RH after stabilization of the first desorption on the corresponding RH levels, while the fourth was an adsorption from the dry state (Fig. 2a to e). This dry state is obtained by an oven-drying at 50 °C, 80 °C and 105 °C respectively until the mass of samples remained constant. The degree of saturation of a sample was classically given by the relationship:

$$Sr = \frac{m - m_0}{m_{sat} - m_0} \tag{3}$$

Where m is the mass at equilibrium, m_0 the dried mass, and m_{sat} the saturated mass.

According to the experimental results (area circled on Fig. 2a and b), a strong fall in the saturation degree was observed between 100% RH and 97% RH. The fact that the samples had a small thickness (0.5 cm) for a large exposed area (3.5 cm × 7 cm) could give the impression that this fall was due to a surface effect. However, the similarity of results with those obtained by Brue [39] for the same materials but on larger samples (cylinders of diameter = 3.75 cm, height = 5 cm) contradicts this hypothesis. In addition, this effect is noted on other isotherms from the literature found at the same temperature but on different materials [20,29]. The drop is also marked on carbonated samples made with different types of cement [29].

Table 5
Distribution of pore volume for 1 m^3 of material.

Materials	C–S–H amount (m^3)	C–S–H gel pores (m^3)	Capillary pores (m^3)	Porous volume (m^3)
C1	0.098	0.027	0.096	0.123
C2	0.115	0.032	0.115	0.147
M	0.094	0.026	0.146	0.172
CP1	0.353	0.099	0.204	0.303
CP2	0.337	0.094	0.311	0.405

The fall of the isotherm at high humidity could be associated with a percolating pore network that drained very quickly, as soon as moisture declined. For this reason, we believe that this part of the pore distribution plays an important role in the water permeability of the saturated material. Assumed to be made up of wide interconnected capillary pores or large pores connected by microcracks, it was modeled by large pores having an average radius related to the intrinsic gas permeability of the material. This is why the capillary pore family was divided into two parts for modeling purposes (as in the Mindess classification). According to the experimental desorption isotherms (Fig. 2a to e), it seems that, for CEMI-based materials, the porosity associated with this percolated capillary pores is about 25 to 30% of the total open porosity. For the concrete C2, it constitutes about 15% of the total porosity.

Between 76 and 97% RH, the degree of saturation of the concrete C2 showed small variations compared to concrete C1. This is quite logical since, in this range of RH, the capillary porosity is affected by water movement [16]. As the concrete C2 contains additives (slag and fly ash), secondary C–S–H are formed by pozzolanic reactions during hydration. The fraction of total porosity associated with capillary pores is therefore reduced. This is not the case for OPC-based concrete. This has been shown recently by Nguyen [36] for blended cements containing silica fume.

From a relative humidity close to 50%, the porosity of C–S–H played an important role. The variation in the degree of saturation of the concrete C1 became smaller compared with that of concrete C2. Concerning the intermediate cycles, it was found that the hysteresis effect became more and more significant as the relative humidity from which adsorption started decreased. This was taken into account in the modeling part by an increase of the connectivity between the fraction of the porous network still filled with water and the fraction already drained away.

2.3.2. Intrinsic gas permeability

Gas permeability was used in this study to obtain the average radius of the large capillary pore family. The intrinsic gas permeability was preferred to water permeability because water has the disadvantage of reacting with the cement paste. It can hydrate the anhydrated cement and also change the chemical equilibria by dissolution, leaching, and/or precipitation of calcite (if the latter is carbonated). Thus, the permeability to water is consistently lower than the permeability measured with gas. Note that ethanol permeability could also be used since it is of the same order of magnitude as the gas permeability [40]. According to [40], the steady state is reached more quickly when the permeability is measured with ethanol. The values of gas permeability used for the modeling of the porous network are listed in Table 6.

The values adopted for concretes C1 and C2 were those obtained by Camps [30] according to the AFPC-AFREM protocol [41]. For mortar M and cement paste CP2, experimental results obtained at LMDC on similar materials with the same protocol were chosen. The gas permeability of CP1 was measured by Baroghel Bouny [42].

3. Modeling

3.1. Pore connectivity

The original model, the principle of which was mentioned in paragraph 1 , was developed by Ishida et al. [18]. On the same basis, the hysteresis effect was represented by the implementation of a pore size distribution in which the pores supposed to be drained at a given RH were taken to be only partially drained. Assuming that drying

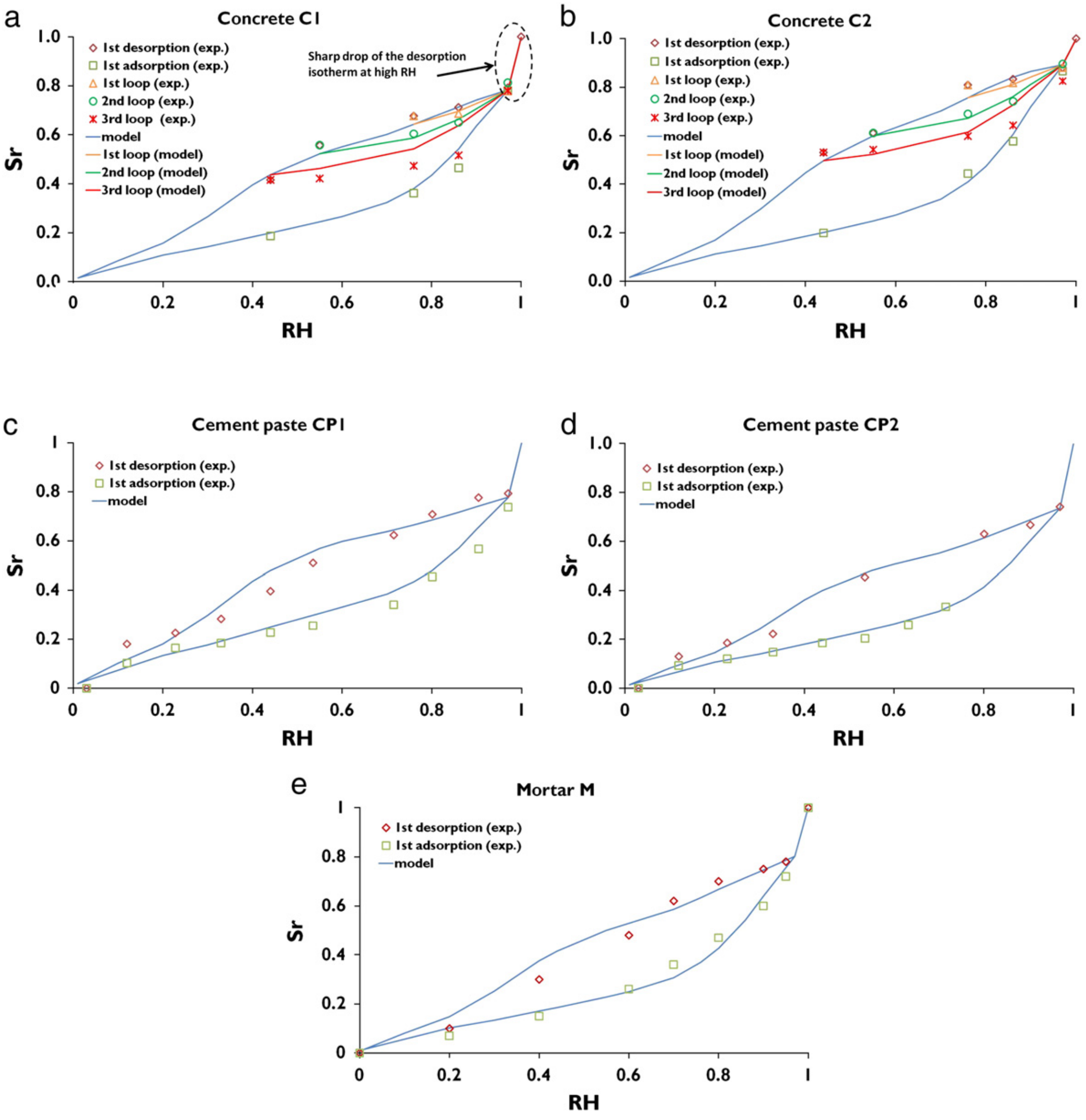

Fig. 2. Experimental results (symbols) and simulated results (solid line).

occurs by vapor diffusion in the unsaturated network, pore drying is then possible when the pore is directly connected to the dry network. As the dried space increases when the RH decreases, the probability of connection of a saturated pore to the dry network increases with drying. This explains the decrease of hysteresis in the range of low relative humidity. First, let us consider that pores are cylindrical. Assuming that drying affects pores with size r_1 when the relative humidity is h_1, the drained portion of the porous network represents a fraction of pores of radius larger than r_1. This fraction depends on the connectivity between the drained portion and pores of radius r_1. It is very likely that, the longer the developed length of pores with radius bigger than r_1, the greater their potential connectivity. In fact, most of these pores are long, so they are able to intercept pores of various sizes. The length of a pore is a concept difficult to handle. Valckenborg et al. [43] have determined the pore size distribution of a mortar by NMR which measures the true pore volume-to-surface area ratio. They highlighted a bimodal distribution with a first peak at 20 nm corresponding to capillary pores and a second peak close to 5 nm corresponding to C–S–H pores. The pore size distribution obtained shows that the pore volume fraction associated to the C–S–H pores is greater than the one associated to the capillary pores. This was confirmed by the pore size distribution determined by other techniques like water vapor adsorption. These results seem to agree with the fact that small pores are long. For this reason, we assume that the probability of interconnection of pores with radius greater than r_1 can be approximated by the ratio between the total length of pores for which $r > r_1$ to the cumulative total length of all pores of the network considered (Eq. (4)).

$$P_c(r > r_1) \approx \frac{\int_{r_1}^{r_{max}} \frac{1}{a(r)} \frac{dV}{d \log r} d \log r}{\int_{r_{min}}^{r_{max}} \frac{1}{a(r)} \frac{dV}{d \log r} d \log r} \quad (4)$$

Table 6
Values of intrinsic gas permeability.

	C1	C2	M	CP1	CP2
K (10^{-17} m^2)	4.0	5.5	2.5	13.0	20.0

Where a(r) is the pore sectional area defined by Eq. (7). dV/dlogr is the density function of the pore size distribution, (approximated by Eq. (21) in the model).

We will see in paragraph 3.4 that the pore size distribution involved in our model has 3 modes which are respectively associated to C–S–H pores, thin capillary pores and large capillary pores. These large capillary pores are assumed to be microcracks which are connected to themselves and are responsible for the sharp drop of the desorption isotherm at high RH as mentioned earlier. Thus for these pores, we can write that P_c $(r>r_1)$ is equal to 1. Eq. (4) is therefore only valid for C–S–H pores and thin capillary pores. We then propose to normalize the function P_c by taking into account the porosities corresponding to each mode. The normalized function is noted as P_c^* and is given by Eq. (22).

In Eq. (5), the term under the integral represents the length associated with the elementary class of pore with radius r.

$$dl = \frac{1}{a(r)}\frac{dV}{d\log r}d\log r \tag{5}$$

If we assume a constant pore volume, the smaller the pore cross-sectional area a(r), the longer the pore. If all pores have cylindrical shapes, the thinnest would have great developed lengths. Of course, they would be able to connect the larger pores and they could lead to considerable hysteresis even at low relative humidity. C–S–H have been characterized as nodules of 60x30x5 nm^3 [44]. Due to its layered structure [44,45], there is no reason to consider cylinders for the fine pores inter-nodules. This leads us to propose a flattened shape for pores with lower radii, approximated by an oblong geometry (Fig. 3).

This kind of pore will be seen by mercury intrusion porosimetry (MIP) or water vapor adsorption as a pore of radius r. This form can be characterized by an aspect ratio A_p, defined as the ratio between the width and the height of the pore section. For the reasons mentioned above, the coefficient A_p evolves to flatten the pores with small radius. An exponential law is proposed to model this (Eq. (6)).

$$A_p(r) = \frac{l}{2r} = \max\left(\exp\frac{r_{cr}}{r};1\right) \tag{6}$$

Where r_{cr} is a calibration parameter called the “critical radius”. This parameter can also be interpreted as the radius below which pores feature a more oblong than cylindrical shape, and could be the threshold between capillary and C–S–H pores.

According to this function, the large pores are cylindrical, as their aspect ratio cannot exceed 1, and the pores become progressively flattened as r decreases.

The cross-sectional area of the pore is

$$a(r) = (4(A_p(r)-1)+\pi)r^2 \tag{7}$$

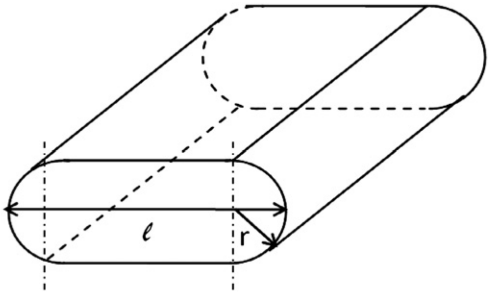

Fig. 3. Oblong shaped pore.

3.2. Adsorption and capillary condensation

At relative humidity h, the pore radius subjected to condensation is given by the relationship:

$$r(h) = r_k(h) + e_a(h) \tag{8}$$

Where $r_k(h)$ and $e_a(h)$ respectively denote the capillary condensate radius and the thickness of adsorbed water on pore walls.

In the case of a cylindrical pore, the capillary condensation radius is given by the Kelvin–Laplace equation

$$r_{k1}(h) = -\frac{2\sigma M_v}{\rho RT\ln(h)} \tag{9}$$

Where σ (N/m) is water/vapor interfacial tension, M_v (kg/mol) the molecular mass of water, ρ (kg/m^3) the water density, R (8.32 J/mol/K) the ideal gas constant and T (K), the absolute temperature.

It is well known that the interfacial tension depends on the ionic concentrations of the pore solution which can also modify the equilibrium of the liquid–vapor interface and consequently the Kelvin relation. This fact was studied for example by Monlouis Bonnaire [46]. We decide to keep the initial relation of Kelvin (Eq. (9)) and to neglect these effects for sake of simplification. For this study, the interfacial tension is only a function of the temperature.

$$\sigma(T) = (128-0.185T)\times10^{-3} \tag{10}$$

A relation adopted by Maekawa et al. [28] is used for the dependence of water density with temperature

$$\rho(T) = 1.54\times10^{-8}T^3 - 1.85\times10^{-5}T^2 + 6.65\times10^{-3}T + 2.47\times10^{-1} \quad (273K < T < 373K) \tag{11}$$

It is clear that Eq. (9) is no longer valid when the pore features a higher surface/volume ratio. When the flattening progresses, the pores are comparable to oblong prisms. The relationship of Kelvin–Laplace tends towards marked flattening

$$r_{k2}(h) = -\frac{\sigma M_v}{\rho RT\ln(h)} \tag{12}$$

The transition from Eqs. (9)–(12) is ensured by (13)

$$r_k(h) = -\frac{(1+\alpha)\sigma M_v}{\rho RT\ln(h)} \tag{13}$$

The term α is a function of the aspect ratio A_p (r_{k1}), $\alpha = 1$ when A_p $(r_{k1}) = 1$ and 0 when A_p $(r_{k1}) = A_{pmax}$. A value of 4 was adopted for A_{pmax}. This allowed us to limit transition from Eqs (9)–(12) (corresponding to the passage of α from 1 to 0) to a small range of pore sizes, in order to be able to neglect the effect of the transition on the isotherm shape without causing singularities during the numerical implementation of the model. It is likely that the oblong shape becomes dominant from an aspect ratio around this value. Moreover whatever the value in this order of magnitude, there is no effect of the value on the results. The expression for α is given by Eq. (14)

$$\alpha = \max\left[1-\left(\frac{A_p(r_{k1})-1}{3}\right);0\right] \tag{14}$$

In Eq. (14), we choose in first order a linear assumption. This is a simplifying hypothesis.

For the expression of $e_a(h)$ used in Eq. (8), the BET model was used [47]. This gives the number of adsorbed water molecule layers n as a function of the relative humidity h and temperature T

$$n = \frac{Ch}{(1-h)[1+(C-1)h]} \tag{15}$$

C is the BET constant depending on temperature

$$C = \exp\left[\frac{E_1 - E_l}{RT}\right] \tag{16}$$

Where E_1 (J/mol) is the molar energy of adsorption of the first layer and E_λ (J/mol), the molar energy of liquefaction of the adsorbate.

C depends on the adsorbate/adsorbent pair. However, for the purposes of this model, we adopted the expression used by Xi et al. [48].

$$C = \exp\left(\frac{855}{RT}\right) \tag{17}$$

$e_a(h)$ is then obtained by multiplying n by a water molecule size ($\sim 3.10^{-10}$ m)

$$e_a(h) = 3 \times 10^{-10} \times n(h) \tag{18}$$

3.3. Hysteresis

If the humidity decreases from h_1 to $h_2 < h_1$, then the pores with radii between $r_1 = r(h_1)$ and $r_2 = r(h_2)$ are partially drained. The residual degree of saturation of pores with radii greater than r_2, noted as S_{ink}, is in the context of the present model, dependent on their connectivity to the dry network. This connectivity is in turn dependent on the probability of interconnection of pores with sizes greater than r_2. Therefore, we propose to adopt the following relationship as a first approximation.

$$S_{ink} = 1 - P_c^*(r > r_2) \tag{19}$$

If the relative humidity increases from h_1 to $h_3 > h_1$ (corresponding to a pore radius r_3), the pores with sizes between r_1 and r_3 belonging to the dry portion of the network are instantly saturated again. Of course, the volume of water present in pores with radius greater than r_3 but drained only via smaller pores, remains constant.

By noting Sr, the degree of saturation of a pore with radius r and $\dot{h}$ the rate of change of relative humidity during the time dt, the mechanisms can be summarized as follows.

$$\begin{array}{l} \text{If } \dot{h} \geq 0 \text{ then} \\ Sr = 1 \ \ \forall r \leq r(h + \dot{h}dt) \\ Sr = 0 \ \ \forall r > r(h + \dot{h}dt) \\ \text{If } \dot{h} < 0 \text{ then} \\ Sr = 1 \ \ \forall r \leq r(h + \dot{h}dt) \\ Sr(t + dt) = \min(S_{ink}, Sr(t)) \ \ \forall r > r(h + \dot{h}dt) \end{array} \tag{20}$$

Eq. (20) is the equation key.

3.4. Numerical implementation

It is clear that the management of saturation increments based on relative humidity increments can be treated easily only on a numerically discretized porous network. To this aim, the pore size distribution was discretized and the probability of inter-connectivity (Eq. (4)) was also approximated by a linear interpolation from one discrete radius to another. This is a simplifying hypothesis.

As explained earlier, it is necessary to consider several modes, respectively associated with the C–S–H gel pores, the thin capillary pores and the large capillary pores. From an analytical point of view, polynomials of degree 2 of log(r) are juxtaposed to represent the distribution. In fact, these polynomials are easily differentiable analytically. Thus, a mode can be represented by four portions of parabola. Each parabola is defined by a range of log(r) with a width equal to δ and a height equal to H/2 on the axis dV/dlog(r) (Fig. 4).

For a distribution containing 3 modes

$$\frac{dV}{d\log r} = \bigcup_{i=1}^{i=3} \left(\bigcup_{j=1}^{j=4} \left(\beta_{ji}^1 (\log r)^2 + \beta_{ji}^2 (\log r) + \beta_{ji}^3 \right) \right) \tag{21}$$

Where the coefficients β_{ji}^k (k = 1 to 3) depend on three parameters: the modal radius $r_{mode\ i}$, the amplitude, δ, and the height H_i.

This simplified representation with three modes allows pore volumes to be calculated analytically and the number of parameters describing the distribution to be limited. Once defined, the modes are discretized as shown in Fig. 4. Beyond 100 discretizations, the number of discretizations has no effect on the simulation results. The model was implemented using the free software SCILAB [49].

3.5. Model calibration

3.5.1. Calibration of modes associated with C–S–H gel pores and thin capillary pores

The pore size distribution used in this model is assumed to be the "real" distribution, not the one obtained from mercury intrusion tests, which is an image of the real distribution. The latter provides only the access radius into a given pore volume. Because of the "ink-bottle effect", this volume may contain large pores that are accessible through smaller ones. Furthermore, the characterization of pore structure by mercury intrusion tests is limited because the finest pores are not accessible due to limitations of the apparatus (access radius limited to around 3 nm).

To comply with the classification proposed by Mindess et al. [38] (see paragraph 2) the following values were imposed: δ = 0.4 associated with a value of r_{mode} fixed at 1.5 nm for the first mode (r_{C-S-H}) and 9.5 nm for the second mode (r_{thin}). In order to limit the number of fitting parameters, a single value of δ was used for the three modes. As discussed in the next section, the value of intrinsic permeability allows the determination of the radius of the mode associated with large connected capillaries (r_{large}). It is assumed that these capillaries play a major role in the permeability; this

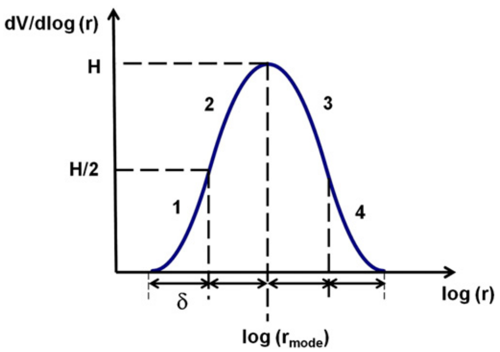

Fig. 4. Mode representation with four portions of parabola.

stage is explained in the following section. Finally, the height h depends directly on the porosity associated with each mode. The porosity was designated by ϕ_1 for the C–S–H, by ϕ_2 for the small capillaries, by ϕ_3 for large capillaries. These porosities are defined in relation to the total volume of the material. The normalized probability of interconnection P_c^* is then defined by Eq. (22).

$$\begin{aligned}
&\text{If } \log r > \log(r_{large}) - 2\times\delta \text{ then}\\
&P_c^*(r > r_1) = 1\\
&\text{Else } \log r < \log(r_{large}) - 2\times\delta \text{ then}\\
&P_c^*(r > r_1) = \frac{1}{\phi}\left[(\phi-\phi_3)\times P_c(r > r_1) + \phi_3\times 1\right]
\end{aligned} \tag{22}$$

3.5.2. Calibration of the third mode associated with large capillary pores

Considering that large capillaries are primarily responsible for the water permeability of saturated material, r_{large} was calibrated according to the intrinsic permeability using a classical permeability model.

Many authors have used the Katz–Thompson relation to determine the liquid permeability through the distribution of pore size obtained by mercury porosimetry [50–52]. Other approaches based on an analytical method [53] or on a pore network model [1,2] have also been developed. However, they involve the results of mercury porosimetry associated with some empirical considerations. Therefore they were not used as part of our model. The simple capillary model developed by Dullien [54] quoted in [55] was adopted. This model consists of calculating the permeability K with a cylindrical pore model involving Poiseuille's law and Darcy's law.

The volume flow q (m^3/s) through a cylindrical pore of radius r (m) is related to the pressure gradient Δp/l by Poiseuille's law

$$q = \frac{\pi r^4}{8\mu}\frac{\Delta p}{l} \tag{23}$$

Where μ (Pa s) is the viscosity of fluid through the pore.

The volume flow Q (m^3/s) through the material is given by Darcy's law

$$Q = \frac{K}{\mu}A\frac{\Delta p}{l} \tag{24}$$

Where A (m^2) is the material cross-sectional area.

The permeability, K, is obtained by setting the volume flow through the material equal to the sum of flows through the pores.

By integrating the tortuosity T, the relationship between the permeability, K, on the one hand and the mode radius r_{large} and porosity ϕ_3 on the other becomes:

$$K = \frac{\phi_3 r_{large}^2}{8T^2} \tag{25}$$

The porosity ϕ_{large} is estimated from the drop of the desorption isotherm at high RH, which is associated to large interconnected capillaries or large pores connected by microcracks.

From Eq. (25), we obtain r_{large} (m)

$$r_{large} = 2T\sqrt{\frac{2K}{\phi_3}} \tag{26}$$

Generally, the tortuosity T is related empirically to the porosity. A relationship attributed to Carniglia [56] is for example used by Aït Mokhtar et al. [2]. Other expressions found by other authors are related by Matyka et al. [57]. Among those proposed, we kept the relation developed by Comiti and Renaud [58] to calculate the tortuosity for fixed beds of parallelepipeds with different thickness-to-side ratios.

$$T(\phi_{large}) = 1 - 0.86\ \ln(\phi_{large}) \tag{27}$$

3.5.3. Calibration of critical radius r_{cr}

The critical radius r_{cr}, defining the transition value between cylindrical and oblong pores was set to 1.6 nm, which is common for all the materials studied. This value was obtained after an inverse analysis. It corresponds to a Kelvin radius for 47% RH at T = 20 °C. Our approach is in agreement with Nguyen [36]. The author distinguishes two distinct areas: one for low values of RH, where the amount of hydrates plays a dominant role in water movement, and a second for high values of RH, where porosity is the most important parameter. These two areas are separated by an RH threshold value of around 44%. In the proposed model, this radius also corresponds to r_{cr}, which is precisely the transition radius between cylindrical and oblong pores.

All the data used in the model for each material tested are summarized in Table 7.

Fig. 5 (a to e) highlights the corresponding pore size distributions.

4. Results and comments

The idealized pore size distribution involved in this study is assessed from parameters which are easily measurable or computable: the degree of hydration, the porosity accessible to water and the intrinsic gas permeability. The other necessary data are the chemical composition of the cement and the formulation of the material. The distribution is represented by elementary functions: polynomials of degree 2. The modal radius values are fixed except that of the mode associated to the coarse pores calibrated from gas permeability. The amplitude of each mode is also fixed. The model is then easy to implement. In the function describing the connectivity of the porous network, which essentially makes the originality of this work, the only residual calibration parameter is the critical radius which corresponds to the transition between cylindrical shape associated to capillary pores and oblong shape associated to C–S–H pores. This value is the same for all the materials studied: 1.6 nm. As seen in Fig. 2a to e, the model realistically reproduces first desorption and first adsorption isotherms and especially the hysteresis loops.

The model can also estimate the specific surface Ss by multiplying pore perimeters by their lengths and summing the results obtained. The theoretical surface can be compared with experimental results (Table 8).

Baroghel Bouny [17] has made measurements of specific surface by the BET method on an ordinary concrete and a high-performance concrete. The BET method aims to quantify the surface accessible to molecules of gas in the pores of a material. The values obtained by the author, with water vapor as adsorbate, are around 20 to 25m^2/g. They are even of the same order of magnitude as the values provided by the model for concretes C1 and C2. For mortar M and cement pastes CP1 and CP2, the model also gives values of the same magnitude as those measured.

Table 7
Data used for each material tested.

	Porosity	$r_{C\text{–}S\text{–}H}$	ϕ_1	r_{thin}	ϕ_2	r_{large}	ϕ_3	δ	r_{cr}
	(%)	(nm)	(%)	(nm)	(%)	(nm)	(%)		(nm)
C1	12.300	1.5	2.700	9.5	6.520	410	3.080	0.4	1.6
C2	14.700		3.200		9.300	580	2.200		
M	17.200		3.280		10.100	225	3.800		
CP1	30.300		9.600		13.700	385	7.000		
CP2	40.500		9.230		16.920	350	11.340		

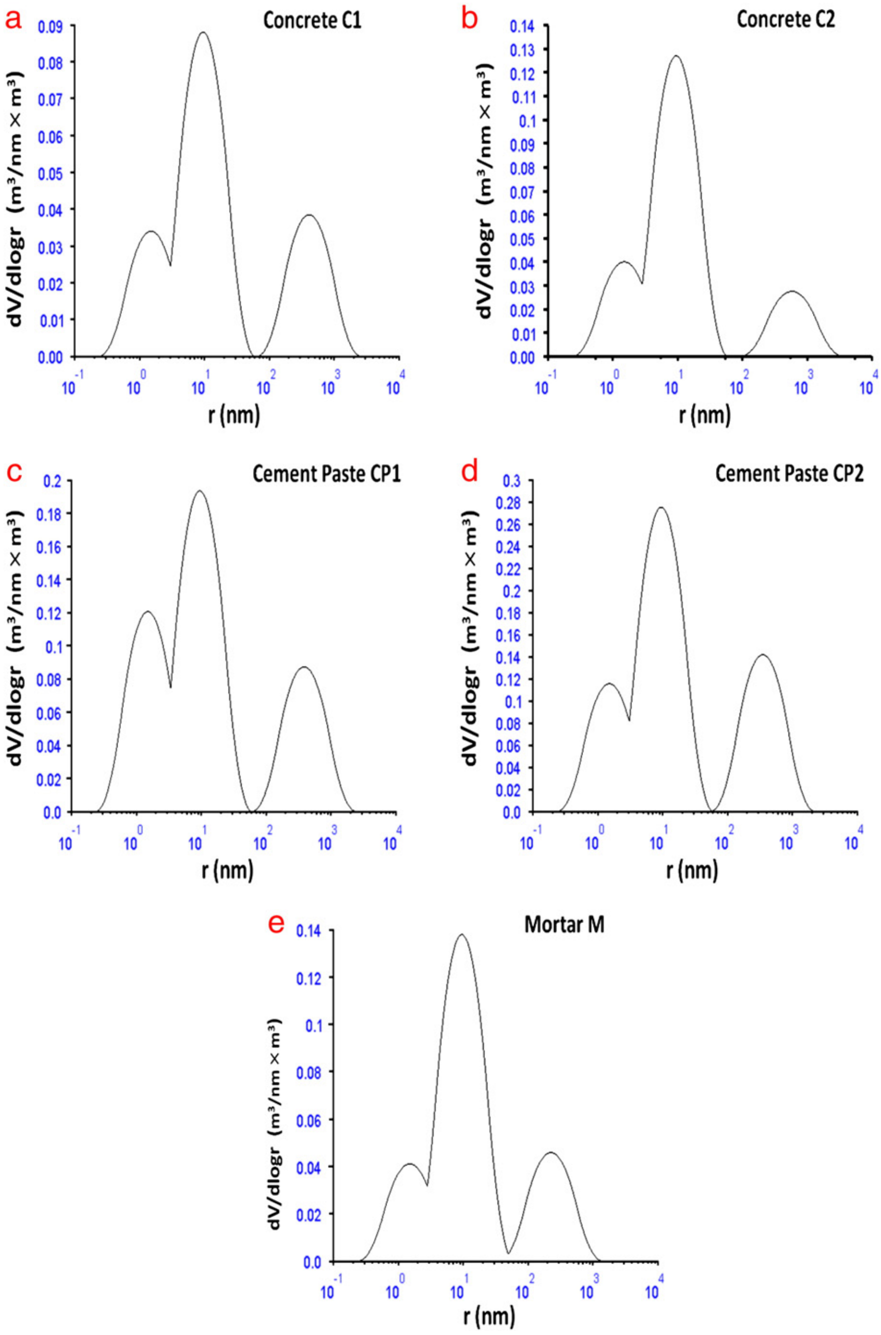

Fig. 5. Proposed pore size distribution for the materials studied.

For comparison, the pore size distributions obtained by mercury intrusion for concretes C1 and C2 are given in Fig. 6. For concrete C1, we can distinguish one mode with an access radius around 50 nm (Fig. 6a). For concrete C2, we have 2 modes whose access radii are respectively 20 and 1000 nm (Fig. 6b). It is likely that the second mode is an artifact because the results obtained by Brue [39] on a similar material don't reveal its presence.

Table 8
Comparison between specific surfaces calculated from the model and experimental specific surfaces.

	Ss model (m^2/g)	Ss exp. (m^2/g)
C1	16.2	20.0–25.0 (BET)
C2	21.2	
M	21.4	31.8 (BET)
CP1	66.2	83.0 (BET)
CP2	80.2	123.0 (BET)

The comparison between the theoretical porosity distribution used in the model (1) with that obtained by mercury intrusion (2) for concretes C1 and C2 are given in Fig. 7. In our case, the mercury porosity gives access only to pores (assumed cylindrical) with radii above 3.8 nm (Fig. 7a and b).

It is not surprising that the mercury porosimetry significantly overestimates the volume of small pores, because of the ink bottle effect. Fig. 7 shows that great quantities of large pores are accessible only through smaller pores. The fineness of the cement used for concrete C2 is also highlighted (proportion of finest pores is greater for C2).

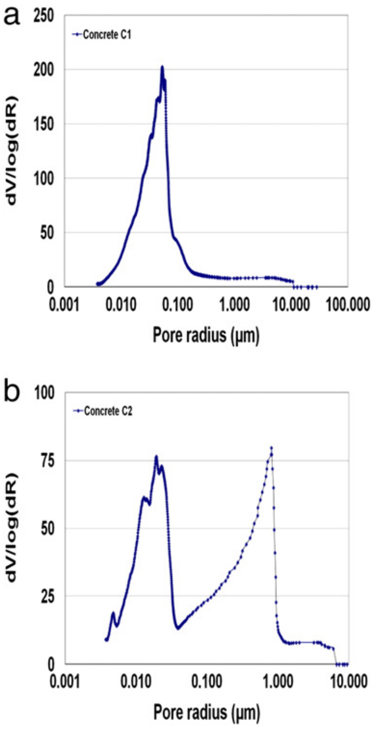

Fig. 6. MIP results for concretes C1 and C2.

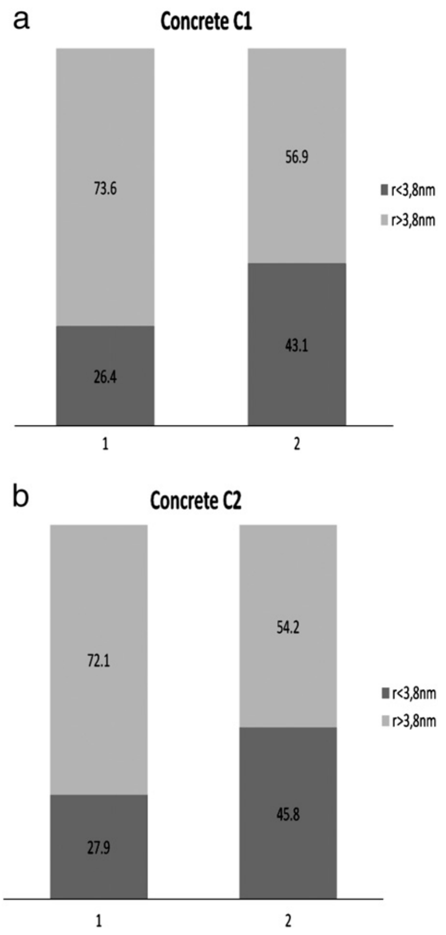

Fig. 7. Theoretical porosity distribution (1) and distribution obtained by mercury intrusion (2).

5. Conclusions

A physical porous network model has been developed for cement-based materials, to simulate the water sorption–desorption isotherms and to predict any hysteresis. Modeling is based on a trimodal pore size distribution. The modes are associated with C–S–H pores, thin capillaries, and large interconnected capillaries or large pores connected by microcracks. It is assumed that the large capillaries form a percolating network responsible for the sharp drop in the saturation degree at high relative humidity in the desorption isotherm. Therefore, they play an essential role in the water permeability of the saturated material. Each mode is characterized by 3 parameters: the mode radius, r_{mode}, the amplitude, δ, and the height, H. The value of δ is fixed at 0.4 (in log(r), with r in nm) with a value of r_{mode} equal to 1.5 nm for the first mode $r_{C–S–H}$ and equal to 9.5 nm for the second mode r_{thin}. For the third mode, r_{large}, the value is calculated from the intrinsic gas permeability. The ethanol permeability can also be used. The height, H is computed from the porosity associated with each mode. The distribution of pore volume between different modes is obtained by calculating the amount of C–S–H formed which constitute the first mode and by using the initial drop in the desorption isotherm to estimate large capillaries. The porosity associated with the central mode is the remaining percentage required to reach the total porosity. The other data used in the model are deduced from the chemical composition of cement, the formulation of the material, the degree of hydration and the open porosity (measured with water as the wetting liquid).

To manage the hysteresis, a function of inter-connectivity is associated with the pore size distribution. This function is then used to calculate the residual saturation due to the ink-bottle effect, assuming that pore drying is only possible if the pore is directly connected to a dry network. The inter-connectivity is approximated by the ratio between the total length of pores affected by drying for a given relative humidity and the total cumulative length of all pores of the network. An oblong geometry is attributed to small pores with a progressive dimensions ratio managed by an aspect ratio involving a parameter noted r_{cr} (critical radius). The value of this parameter, obtained by inverse analysis, is set to 1.6 nm, a common value for all the materials studied. This value corresponds to the transition size between cylindrical pores and oblong pores. The conditions for changing the degree of saturation are then numerically managed on a discretized network.

The simulations were performed on one concrete, one mortar and two cement pastes made with OPC and on a concrete made with Portland–Slag–Fly ash-cement. The results obtained show that, with only one fitting parameter (r_{cr}) common to all the material, the model adequately restitutes the experimental results, in particular the hysteresis loops. On the other hand, the values of specific surface area calculated using the model are of the same order of magnitude as those measured experimentally by the BET method.

The next step is to extend the model to predict isotherms (i) on leached or carbonated materials by changing the pore size distribution and (ii) at high temperature (taking into account the dependence of the connectivity with temperature). The prediction of water sorption isotherms on early aged materials by the model is also an interesting perspective to this study. For this purpose, an evolution law of the degree of hydration could be proposed. In this case, an adjustment of the parameters which define each mode on the pore size distribution is of course necessary.

Acknowledgement

We wish to express our thanks to Andra (French National Agency for Radioactive Waste Management) for its scientific and financial support to the project that led to the development of this model.

References

[1] D. Breysse, B. Gerard, Modelling of permeability of cement based materials, Part I: uncracked medium, Cement and Concrete Research 27 (5) (1997) 761–775.

[2] A. Aït-Mokhtar, O. Amiri, P. Dumargue, S. Sammartino, A new model to calculate water permeability of cement based materials from MIP results, Advances in Cement Research 14 (2) (2002) 43–49.

[3] O. Amiri, A. Aït-Mokhtar, M. Sarhani, Tri-dimensional modelling of cementitious materials permeability from polymodal pore size distribution obtained by mercury intrusion porosimetry test, Advances in Cement Research 17 (1) (2005) 39–45.

[4] G. Ye, P. Lura, K. van Breugel, Modelling of water permeability in cementitious materials, Materials and Structures 39 (9) (2006) 877–885.

[5] H.W. Song, S.J. Kwon, Permeability characteristics of carbonated concrete considering capillary pore structure, Cement and Concrete Research 37 (6) (2007) 909–915.

[6] J.P. Monlouis Bonnaire, J. Verdier, B. Perrin, Prediction of the relative permeability to gas flow of cement based materials, Cement and Concrete Research 34 (5) (2004) 737–744.

[7] B. Pradhan, M. Nagesh, B. Bhattacharjee, Prediction of the hydraulic diffusivity from pore size distribution of concrete, Cement and Concrete Research 35 (9) (2005) 1724–1733.

[8] S. Bejaoui, B. Bary, Modeling of the link between microstructure and effective diffusivity of cement pastes using a simplified composite model, Cement and Concrete Research 37 (3) (2007) 469–480.

[9] R. Võcka, C. Gallé, M. Dubois, P. Lovera, Mercury intrusion porosimetry and hierarchical structure of cement pastes, Cement and Concrete Research 30 (4) (2000) 521–527.

[10] A. Laventis, D.A. Verganelakis, M.R. Halse, J.B. Webber, J.H. Strange, Capillary imbibition and pore characterisation in cement pastes, Transport in Porous Media 39 (2) (2000) 143–157.

[11] K. Aligizaki, Pore structure of cement based-materials: testing, interpretation and requirements, Modern Concrete Technology 12, Spon Press, 2006.

[12] J.H. de Boer, The shapes of capillaries, in: D.H. Everett, F.S. Stone (Eds.), The Structure and Properties of Porous Materials, in Proceedings of the Tenth Symposium, Colston Research Society University of Bristol, Butterworths Science Publications, London, 1958, pp. 68–94.

[13] K.S.W. Sing, D.H. Everett, R.A.W. Haul, L. Moscou, R.A. Pierotti, J. Rouquérol, T. Siemieniewska, Reporting physisorption data for gas/solid systems with special reference to the determination of surface area and porosity, Pure and Applied Chemistry 57 (4) (1985) 603–619.

[14] J.W. Mc Bain, An explanation of hysteresis in the hydration and dehydration of gels, Journal of the American Chemical Society 57 (4) (1935) 699–700.

[15] S. Brunauer, R. Sh Mikhail, E.E. Bodor, Some remarks about capillary condensation and pore structure analysis, Journal of Colloid and Interface Science 25 (3) (1967) 883–892.

[16] V. Baroghel Bouny, Water vapour sorption experiments on hardened cement based materials, Part I: essential tool for analysis of hygral behaviour and its relation to pore structure, Cement and Concrete Research 37 (3) (2007) 414–437.

[17] V. Baroghel Bouny, Caractérisation des pâtes de ciment et des bétons : Méthodes, analyse, interprétations, PhD Thesis, Ecole Nationale des Ponts et Chaussées, 1994.

[18] T. Ishida, K. Maekawa, T. Kishi, Enhanced modeling of moisture equilibrium and transport in cementitious materials under arbitrary temperature and relative humidity history, Cement and Concrete Research 37 (4) (2007) 565–578.

[19] S. Poyet, Experimental investigation of the effect of temperature on the first desorption isotherm of concrete, Cement and Concrete Research 39 (11) (2009) 1052–1059.

[20] R.M. Espinosa, L. Franke, Influence of the age and drying process on pore structure and sorption isotherms of hardened cement paste, Cement and Concrete Research 36 (10) (2006) 1969–1984.

[21] P.C. Philippi, H.A. Souza, Modelling moisture distribution and isothermal transfer in a heterogeneous porous material, International Journal of Multiphase Flow 21 (4) (1997) 667–691.

[22] B. Bary, A polydispersed particle system representation of the porosity for non saturated cementitious materials, Cement and Concrete Research 36 (11) (2006) 2061–2073.

[23] J. Carmeliet, F. Descamps, G. Houvenaghel, A multiscale network model for simulating moisture transfer properties of porous media, Transport in Porous Media 35 (1) (1999) 67–88.

[24] M. Hilpert, R. Glantz, T. Miller Cass, Calibration of pore-network model by a pore-morphological analysis, Transport in Porous Media 51 (3) (2003) 267–285.

[25] B. Ahrenholz, J. Tölke, P. Lehmann, A. Peters, A. Kaestner, M. Krafczyk, W. Durner, Prediction of capillary hysteresis in a porous material using lattice-Boltzmann methods and comparison to experimental data and a morphological pore network model, Advances in Water Resources 31 (9) (2008) 1151–1173.

[26] D. Quenard, H. Sallee, Water vapour adsorption and transfer in cement based materials: a network simulation, Materials and Structures 25 (153) (1992) 515–522.

[27] R.M. Espinosa, L. Franke, Ink-bottle pore method: prediction of hygroscopic water content in hardened cement paste at variable climatic conditions, Cement and Concrete Research 36 (10) (2006) 1954–1968.

[28] K. Maekawa, T. Ishida, Multi-scale modeling of structural concrete, 2009.

[29] N. Hyvert, Application de l'approche probabiliste à la durabilité des produits préfabriqués en béton, PhD Thesis, Université de Toulouse, 2009.

[30] G. Camps, Etude des interactions chemo-mécaniques pour la simulation du cycle de vie d'un élément de stockage en béton, PhD Thesis, Université de Toulouse, 2009.

[31] V. Waller, Relations entre composition des bétons, exothermie en cours de prise et résistance en compression. PhD thesis, Ecole Nationale des Ponts et Chaussées. 1999.

[32] T.C. Powers, T.L. Brownyard, Studies of the physical properties of hardened Portland cement paste, Research Bulletin 22, Portland Cement Association, Chicago, IL (1948) Reprint from Journal of the American Concrete Institute in Proceedings 43 (1947).

[33] F. Adenot, Durabilité du béton : caractérisation et modélisation des processus physiques et chimiques de dégradation du ciment. PhD Thesis, Université d' Orléans. 1992.

[34] B. Bary, A. Sellier, Coupled moisture-carbon dioxide-calcium transfer model for carbonation of concrete, Cement and Concrete Research 34 (10) (2004) 1859–1872.

[35] I.G. Richardson, The nature of C–S–H in hardened cement, Cement and Concrete Research 29 (8) (1999) 1131–1147.

[36] M.D. Nguyen, Modélisation des couplages entre hydratation et dessiccation des matériaux cimentaires à l'issue du décoffrage, Etude de la dégradation des propriétés de transfert, PhD Thesis, Ecole Nationale des Ponts et Chaussées, 2009.

[37] H.F.W. Taylor, Cement Chemistry, Academic Press, London, 1990.

[38] S. Mindess, J.F. Young, D. Darwin, Concrete, 2nd EditionPrentice Hall, Englewood Cliffs, NJ, 2002.

[39] F. Brue, Rôles de la température et de la composition sur le couplage thermo-hydro-mécanique des bétons, PhD Thesis, Ecole Centrale de Lille.

[40] H. Loosveldt, Z. Lafhaj, F. Skoczylas, Experimental study of gas and liquid permeability of a mortar, Cement and Concrete Research 32 (9) (2002) 1357–1363.

[41] AFPC-AFREM, Durabilité des bétons, Compte rendu des journées techniques « Méthodes recommandées pour la mesure des grandeurs associées à la durabilité », Toulouse, 1997.

[42] V. Baroghel Bouny, Water vapour sorption experiments on hardened cement based materials, Part II: Essential tool for assessment of transport properties and for durability prediction, Cement and Concrete Research 37 (3) (2007) 414–437.

[43] R.M.E. Valckenborg, L. Pel, K. Hazrati, K. Kopinga, J. Marchand, Pore water distribution in mortar during drying as determined by NMR, Materials and Structures 34 (10) (2001) 599–604.

[44] A. Nonat, The structure and stoichiometry of C–S–H, Cement and Concrete Research 34 (9) (2004) 1521–1528.

[45] H.F.W. Taylor, Proposed structure for calcium silicate hydrate gel, Journal of the American Ceramic Society 69 (6) (1986) 464–467.

[46] J.P. Monlouis Bonnaire, Modélisation numérique des transferts couplés air-eau-sel dans les matériaux cimentaires et les terres cuites, PhD Thesis, Université Paul Sabatier, 2003.

[47] S. Brunauer, P.H. Emmett, E.J. Teller, Adsorption of gases in multimolecular layers, Journal of the American Chemical Society 6 (1938) 309.

[48] Y. Xi, Z.P. Bazant, H.M. Jennings, Moisture diffusion in cementitious materials, Advanced Cement Based Materials 1 (6) (1994) 248–257.

[49] www.scilab.org.

[50] A.S. El Dieb, R.D. Hooton, Evaluation of the Katz Thompson model for estimating the water permeability of cement based materials from mercury intrusion porosimetry data, Cement and Concrete Research 24 (3) (1994) 443–455.

[51] L. Cui, J.H. Cahyadi, Permeability and pore structure of OPC paste, Cement and Concrete Research 31 (2) (2001) 277–282.

[52] M.R. Nokken, R.D. Hooton, Using pore parameters to estimate permeability or conductivity of concrete, Materials and Structures 41 (1) (2008) 1–16.

[53] J.J. Zheng, X.Z. Zhou, Analytical method for prediction of water permeability of cement paste, ACI Materials Journal 105 (2) (2008) 200–208.

[54] F. Dullien, Porous media fluid transport and pore structure, New York Academic Press, 1979.

[55] J.P. Ollivier, J.M. Torrenti, La structure poreuse des bétons et les propriétés de transfert, in La durabilité des bétons sous la direction de Ollivier J.P, Vichot A, 2008.

[56] S.C. Carniglia, Construction of the tortuosity factor from porosimetry, Journal of Catalysis 102 (2) (1986) 401–418.

[57] M. Matyka, A. Khalili, Z. Koza, Tortuosity-porosity relation in the porous media flow, Physical Review E 78 (2) (2008) 1–8.

[58] J. Comiti, M. Renaud, A new model for determining mean structure parameters of fixed beds from pressure drops measurements: application to beds packed with parallelepipedal particles, Chemical Engineering Sciences 44 (7) (1989) 1539–1545.